

AD-A072 996

AIR FORCE GEOPHYSICS LAB HANSCOM AFB MA
A CASE STUDY OF S3-2 OBSERVATIONS IN THE LATE EVENING AURORAL O--ETC(U)

F/G 4/1

JAN 79 W J BURKE, D A HARDY, F J RICH

UNCLASSIFIED

AFGL-TR-79-0011

NL

1 OF 1

AD
A072996



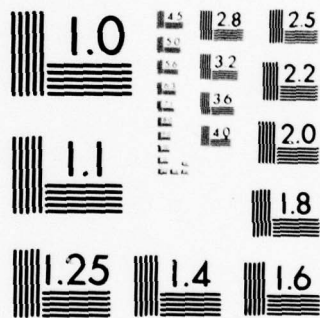
END

DATE

FILMED

9-79

DDC



MICROCOPY RESOLUTION TEST CHART
NATIONAL BUREAU OF STANDARDS-1963-A

DA072996

LEVEL II

AFGL-TR-79-0011
ENVIRONMENTAL RESEARCH PAPERS, NO. 651

12
P.S.



A Case Study of S3-2 Observations in the Late Evening Auroral Oval

W. J. BURKE
D. A. HARDY, Capt, USAF
F. J. RICH
M. C. KELLEY
M. SMIDY
B. SHUMAN
R. C. SAGALYN
R. P. VANCOUR
P. J. L. WILDMAN
S. T. LAI
J. BASS

DDC
REF ID: A61111
AUG 23 1979
RECEIVED
C

8 January 1979

Approved for public release; distribution unlimited.

DDC FILE COPY

SPACE PHYSICS DIVISION PROJECT 2311
AIR FORCE GEOPHYSICS LABORATORY
HANSCOM AFB, MASSACHUSETTS 01731

AIR FORCE SYSTEMS COMMAND, USAF

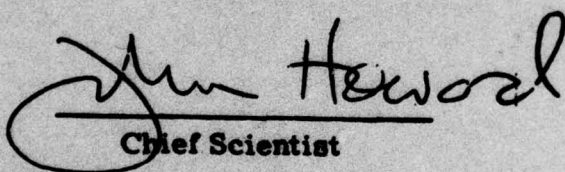


79 08 22 008

This report has been reviewed by the ESD Information Office (OI) and is releasable to the National Technical Information Service (NTIS).

This technical report has been reviewed and is approved for publication.

FOR THE COMMANDER


Chief Scientist

Qualified requestors may obtain additional copies from the Defense Documentation Center. All others should apply to the National Technical Information Service.

9 Environmental research papers

Unclassified

SECURITY CLASSIFICATION OF THIS PAGE (When Data Entered)

REPORT DOCUMENTATION PAGE		READ INSTRUCTIONS BEFORE COMPLETING FORM	
1. REPORT NUMBER	2. GOVT ACCESSION NO.	3. RECIPIENT'S CATALOG NUMBER	
14 AFGL-TR-79-0011, AFGL-ERP-651			
4. TITLE (and Subtitle)	5. TYPE OF REPORT & PERIOD COVERED		
6 A CASE STUDY OF S3-2 OBSERVATIONS IN THE LATE EVENING AURORAL OVAL	Scientific. Interim.		
6. PERFORMING ORG. REPORT NUMBER		8. CONTRACT OR GRANT NUMBER(s)	
10 7. AUTHOR(s) W. J. Burke, F. J. Rich, R. C. Sagalyn D. A. Hardy, M. C. Kelley, R. P. Vancour M. Smiddy, P. J. L. Wildman B. Shuman, S. T. Lai, J. Bass			
9. PERFORMING ORGANIZATION NAME AND ADDRESS Air Force Geophysics Laboratory (PH) Hanscom AFB Massachusetts		10. PROGRAM ELEMENT, PROJECT, TASK AREA & WORK UNIT NUMBERS 61102F 2311G2AE	
11. CONTROLLING OFFICE NAME AND ADDRESS Air Force Geophysics Laboratory (PH) Hanscom AFB Massachusetts 01731		12. REPORT DATE 8 Jan 1979	
14. MONITORING AGENCY NAME & ADDRESS (if different from Controlling Office)		13. NUMBER OF PAGES 41	
		15. SECURITY CLASS. (of this report) Unclassified	
16. DISTRIBUTION STATEMENT (of this Report) Approved for public release; distribution unlimited.		15a. DECLASSIFICATION/DOWNGRADING SCHEDULE	
17. DISTRIBUTION STATEMENT (of the abstract entered in Block 20, if different from Report)			
18. SUPPLEMENTARY NOTES * Regis College, Weston, MA 02193 ** Cornell U., Ithaca, NY 14853 *** Logicon Inc., Hartwell Ave., Lexington, MA 01730			
19. KEY WORDS (Continue on reverse side if necessary and identify by block number) Aurorae S3-2 satellites Electric fields Magnetic fields Electron spectrometer			
20. ABSTRACT (Continue on reverse side if necessary and identify by block number) Instrumentation aboard the polar-orbiting Air Force satellite S3-2, as well as the methods by which the measurements are reduced to geophysically significant quantities, are described in great detail. The quality of the high-time resolution data is illustrated using measurements of an auroral zone overpass in the late evening sector when simultaneous DMSP imagery was also available. The validity of the data reduction processes is corroborated by a detailed comparison of simultaneous measurements of the entire complement of scientific experiments on the satellite.			

DD FORM 1 JAN 73 1473 EDITION OF 1 NOV 65 IS OBSOLETE

Unclassified

SECURITY CLASSIFICATION OF THIS PAGE (When Data Entered)

409 578

50B

Accession For	
NTIS GRA&I	<input checked="checked" type="checkbox"/>
DDC TAB	<input type="checkbox"/>
Unannounced	<input type="checkbox"/>
Justification	
By _____	
Distribution/ _____	
Availability Codes	
Dist	Avail and/or special
A	

Contents

1. INTRODUCTION	5
2. SCIENTIFIC EXPERIMENTS	7
2.1 Electric Field	7
2.2 Magnetic Field	13
2.3 Energetic Electron Spectrometer	15
2.4 Ion Drift Meter	17
2.5 Thermal Electron	19
3. OBSERVATIONAL RESULTS FOR CASE STUDY	20
3.1 Overview	21
3.2 Region 1	27
3.3 Region 2	29
3.4 Region 3	31
4. CONCLUSIONS	35
REFERENCES	37
APPENDIX A: Electric Field Components at 60647 UT	39

Illustrations

1. Artist's Conception of S3-2	6
2. Reduction of Data from the Spinning Dipole	9
3. (a) Satellite Coordinate System Used in this Paper. (b) Phase Angle ψ as Function of E_y/E_z Near 60600 UT.	11

Illustrations

4. Energetic Electron Spectrometer	16
5a. External Configuration of the Ion Drift Meter Experiment	18
5b. Schematic of Boom-mounted, Thermal Electron Probe	18
6. Defense Meteorological Satellite Program Imagery for an Auroral Form Taken ~ 14 Minutes Prior to S3-2 Overpass	22
7. Auroral Electrojet (AE) Index and Dixon Island Magnetogram Components for 11 January 1976	23
8. Simultaneous Measurements of (a) Current to Ion Sensor 2; (b) Ion Density; (c) 5-sec Averaged Values of the Electric Field; and (d) Directional Electron Flux	24
9. Differences Between Measured Magnetic Field Components and the Corresponding IGRF Values: (a) Spin Axis Component in Magnetometer Coordinates; (b) North-South, East-West and Up-down Components in Geodetic Coordinates	24
10. Current Densities Calculated from Variations of ΔB_y (Figure 9a)	24
11. High-time Resolution Measurements of ΔB_y , the Current Measured by the Thermal Electron Probe and the Energetic Electron Directional Flux	29
12. Current Measurements by the Ion Drift Sensors 1 and 3 Near 60646 UT	31
13. Measurements in Region 3 as Functions of UT and Λ	32
14. Electron Spectra Measured in Region 3	33
15. Schematic Representation of the S3-2 Ion Drift Meter Orientation at 6064 UT	41
16. Orientation of the Electric Field Dipole at 60647.5 UT	41

A Case Study of S3-2 Observations in the Late Evening Auroral Oval

1. INTRODUCTION

There has been an enormous effort over the past fifteen years to understand the electrodynamics of auroral phenomena. Physical information has been garnered using ground based as well as balloon, rocket and satellite borne instrumentation. The measurements have been of electromagnetic radiation, energetic particle fluxes, current systems and electric fields associated with aurorae. The scope and limitations of the various measurements and kinds of measurements are well-recognized. The chief limitations relate either to the number of simultaneously measured quantities or to the spatial extent and resolution of the measurements. Limitations of the first kind affect the inputs available for solving the coupled Boltzmann and Maxwell equations. The second kind of limitation concerns the relative capabilities of rocket and satellite experiments. It is common wisdom that fine resolution measurements can be made over short distances using rockets, and only structures spread over great distances may be observed by means of satellites.

The scientific package aboard the U. S. Air Force satellite S3-2 (Figure 1) was designed to mitigate both of these limitations by providing high-time resolution, simultaneous measurements of energetic electron fluxes, thermal plasma characteristics, field-aligned currents and electric fields. It should be recognized that

(Received for publication 5 January 1979)

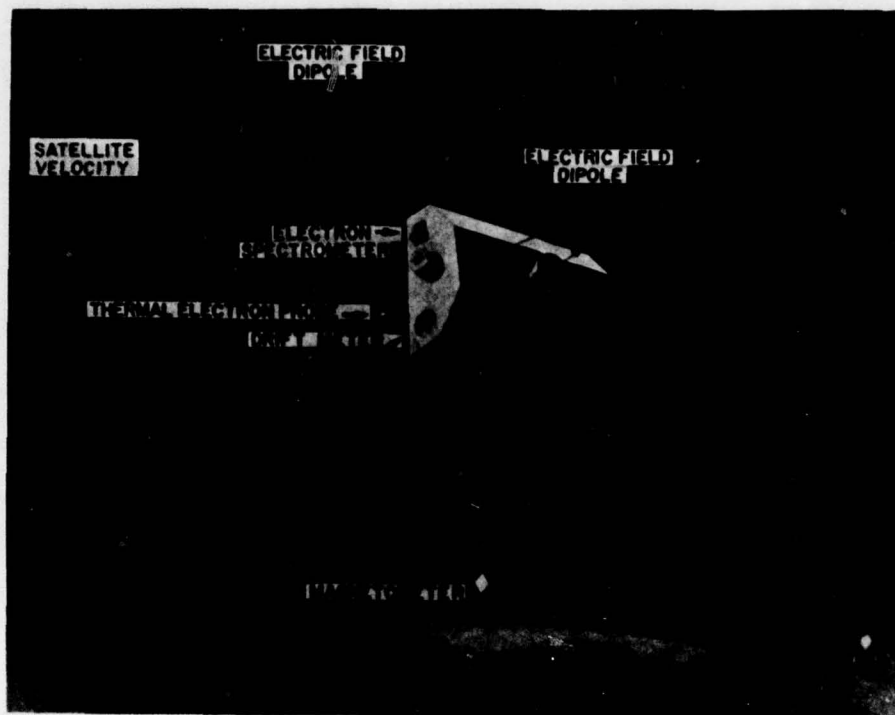


Figure 1. Artist's Conception of S3-2. As viewed in this picture the satellite is spinning in a clockwise sense. The locations of the various instruments are indicated.

the total time derivative of a physical quantity A measured by means of satellite instrumentation is of the form

$$\frac{dA}{dt} = \frac{\partial A}{\partial t} + \vec{V}_s \cdot \nabla A$$

where \vec{V}_s is the velocity of the satellite. The first term is due to temporal changes in the quantity, whereas the second term is due to the spatial variations of the quantity along the satellite trajectory. Without nearby simultaneous measurements, it is not possible to distinguish between spatial and temporal variations. For the sake of simplicity, we assume that the physical quantities measured by S3-2 vary spatially; that is, variations occur on time scales that are long in comparison with the time required by the satellite to cross an auroral feature.

The purpose of this paper is to provide, in a single place, a relatively complete description of the satellite's instrumentation and to illustrate by means of a

detailed example the physical quantities derivable from measurements of the instruments. The paper is meant as a primer for would-be users of the satellite's measurements. It is not meant to be a scientific treatise on the aurora. Physical quantities such as electron fluxes, parallel currents and electric fields are known to be associated with aurorae. We seek only to show what S3-2 instruments can (and cannot) measure. For this reason, many of the references to the work of other investigators are omitted. What references are cited serve to support the reasonability of our claims about some measured quantity. No attempt is made to relate the measurements to the current state of physical understanding of auroral processes.

The paper has two main sections: The first contains a description of each of the instruments and the means by which physically significant quantities are derived from raw measurements; the second section presents a detailed example of S3-2 orbit 517 measurements taken in the late evening sector of the northern auroral oval. This particular S3-2 pass was chosen for presentation because of the availability of nearly simultaneous measurements by a Defense Meteorological Satellite Program (DMSP) optical imager. A brief overview of the observations show that in this case, the auroral oval may be divided phenomenologically into three distinct regions of (1) the diffuse aurora, (2) the strong return current of a visible arc, and (3) the discrete arc (or arcs). Observations from the three regions are then treated in detail.

2. SCIENTIFIC EXPERIMENTS

The Air Force scientific satellite S3-2 was launched into polar orbit in December 1975, with an initial apogee, perigee and inclination of 1557 km, 240 km and 96.3° , respectively. It is spin-stabilized with a nominal spin period of 20 sec, and a spin axis that is nearly perpendicular to the orbital plane in a cartwheel sense. The scientific package carried by S3-2 includes: (1) a dc electric field experiment, (2) a triaxial fluxgate magnetometer, (3) an energetic electron spectrometer, (4) an ion drift meter, and (5) a thermal electron probe. In this section, we describe the instruments and the methods by which their measurements are reduced to give geophysically significant quantities.

2.1 Electric Field

The electric field experiment on S3-2 was designed to consist of three orthogonal dipoles: two in the spin plane and one along the spin axis. Unfortunately, one of the dipoles in the spin plane failed to deploy. The dipole in the spin plane consists of two carbon coated spheres of 3.81-cm radius placed at the ends of

13.72-m insulated cable booms. The spin axis aligned dipole also consists of two spheres held at the ends of 11-m tip to tip rigid booms. The experiment operates in a repetitive 512-sec cycle that begins with a 10-sec calibrate sequence. The probes at the ends of the booms are shorted to satellite ground for one-sec intervals beginning at 128, 256, and 384 sec into the cycle. During the operating portions of the cycle, the potential differences between the ends of the two dipoles are measured 64 times a sec and interpreted using techniques given by Storey¹ and Fahleson.² It has been found that the spin axis aligned dipole is subject to time varying contact potentials. For this reason the measurements are usually limited to those of a single spinning dipole which is not disturbed by such effects. Two scientific papers reporting preliminary results from this instrument have been published.^{3, 4}

The method used to calculate the projection of the ambient electric field into the spin plane of the satellite is illustrated in Figure 2. Here we have plotted the measured potential between the ends of the spinning dipole (panel a), the potential due to the cross-magnetic field motion of the satellite ϕ_v (panel b), the potential due to the ambient electric field ϕ_e (panel c), and the function to which ϕ_e is fitted ϕ_{fit} , and its residues $\phi_e - \phi_{fit}$ (panel d) as functions of universal time in seconds of day and invariant latitude, Λ . The data were taken during S3-2 orbit 517 as the satellite was moving poleward over the late evening sector (~ 2250 LT) of the northern auroral zone. The measured potential across the dipole is of the form

$$\phi_m = \phi_{dc} + \phi_v + \phi_e \quad (1)$$

where ϕ_{dc} is the contribution due to different contact potentials of the two spheres; ϕ_{dc} is easily rejected by considering the amplitudes of the sine waves and not their dc level; ϕ_v is determined using the International Geomagnetic Reference Field (IGRF, 1975) model updated to the epoch of measurements and precisely determined ($<0.5^\circ$ error) spacecraft attitude information. To obtain ϕ_e , the potential due to the ambient electric field, ϕ_v is then subtracted from ϕ_m . In regions where the

1. Storey, L. R. O. (1963) The design of an electric dipole antenna for VLF reception within the ionosphere, Tech. Rep. No. 308 TC, Centre National d'Etudes des Telecommunication, Paris.
2. Fahleson, U. V. (1967) Theory of electric field measurements conducted in the magnetosphere with electric probes, *Space Sci. Rev.* 7:238.
3. Smiddy, M., Kelley, M. C., Burke, W., Rich, F., Sagalyn, R., Shuman, B., Hays, R., and Lai, S. (1977) Intense poleward directed electric fields near the ionospheric projection of the plasmopause, *Geophys. Res. Lett.* 4:543.
4. Burke, W. J., Kelley, M. C., Sagalyn, R. C., Smiddy, M., and Lai, S. (1979) Polar cap electric field structures with a northward interplanetary magnetic field, *Geophys. Res. Lett.* 6:21-24.

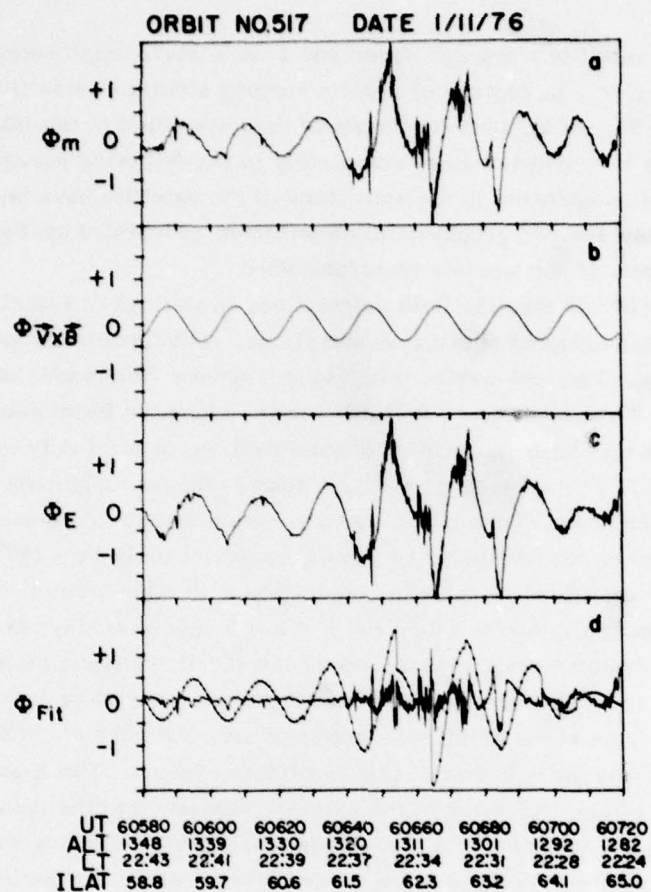


Figure 2. Reduction of Data from the Spinning Dipole. (a) Measured potential difference between the ends of the dipole. (b) Potential due to the $V \times B$ motion of the satellite. (c) The difference between the measured and the $V \times B$ motion. (d) The function to which ϕ_e has been fit and its residues. The data were taken during S3-2 orbit 517 and plotted as functions of universal time (seconds of the day), altitude, invariant latitude, magnetic local time, geographic latitude and longitude

electric field varies slowly over a satellite spin period (for example, prior to 60630 UT, Figure 2) 20 seconds of ϕ_e data are fit to a function of the form

$$\phi_{fit} = \phi \cos(\Omega_s t - \Psi) \quad (2)$$

where Ω_s is the satellite's angular speed and Ψ is a phase angle determined in the fitting procedure. In regions of rapidly varying electric fields (for example, after 60630 UT, Figure 2), only 5 seconds of data are fitted to the function given in Eq. (2). This is discussed more completely in the following paragraphs. Once the electric field components in the spin plane of the satellite have been determined, their values in any desired geophysically significant coordinate systems may be computed by means of appropriate transformations.

The validity of our electric field calculations in regions of rapidly varying fields depends on additional physical assumptions. The basic assumption we use is based on a high classical conductivity along magnetic field lines, which implies that $\vec{E} \cdot \vec{B} = 0$. We ask what potential differences along the boom should be measured if \vec{E} varies with time in magnitude and direction, subject only to the constraint $\vec{E} \cdot \vec{B} = 0$. The subsequent analysis shows that the magnitude ϕ_e in Eq. (2) varies but that the phase of the boom signal at which maximum potential differences are measured either varies slowly or jumps discontinuously by $\sim 180^\circ$. The residues may be examined visually in conjunction with other simultaneous measurements to identify regions in which the $\vec{E} \cdot \vec{B} = 0$ condition may not be valid.

In order to examine the consequences of the $\vec{E} \cdot \vec{B} = 0$ assumption for the potential difference measurements of a rotating dipole, we adopt a system of coordinates with origin at the satellite's center of mass (Figure 3). The spin axis of the satellite is along the Y axis of the coordinate system. The X axis is defined as the direction of the projection of the satellite velocity into the spin plane \vec{V}_p . The Z axis is in the direction of $\hat{x} \times \hat{y}$. Thus if the orbit were circular with a 90° inclination, (X, Y, Z) would be positive toward (north, west, up) during the portion of orbit 517 under consideration. In this paper, we use the subscript p to indicate the projection of a vector into the spin plane. This projection of an arbitrary vector \vec{A} is defined by

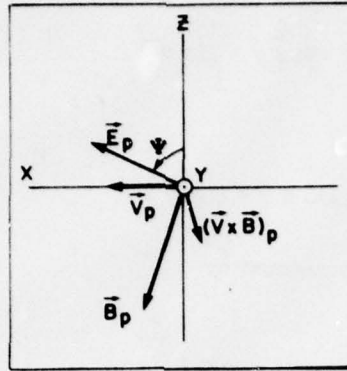
$$\vec{A}_p = -\hat{y} \times (\hat{y} \times \vec{A}) \quad (3)$$

The projections of the electric field, magnetic field and $(\vec{V}_s \times \vec{B})$ near 60600 UT (arbitrary lengths) are also indicated in Figure 3.

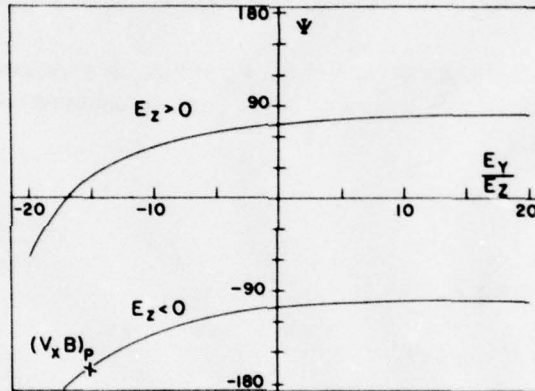
In the spacecraft coordinate system, the magnetic field can be represented as

$$\vec{B} = B (\sin \theta \cos \phi \hat{x} + \sin \theta \sin \phi \hat{y} + \cos \theta \hat{z}) \quad (4)$$

where the azimuth and colatitude angles are defined by $\phi = \tan^{-1} (B_y/B_x)$ and $\theta = \cos^{-1} (B_z/B)$, respectively. In order to study the properties of a vector perpendicular to \vec{B} , we define a set of orthonormal vectors $\hat{e}_1, \hat{e}_2, \hat{e}_3$ such that $\vec{B} = B \hat{e}_3$. This transformation is effected by two rotations. It can easily be shown that



(a)



(b)

Figure 3. (a) Satellite Coordinate System Used in this Paper. Vector quantities (arbitrary scale) marked with subscript p represent projections into the spin plane of the satellite. The -Y axis corresponds to the satellite spin axis. (b) Phase Angle Ψ as a Function of E_y/E_z Near 60600 UT. Projection of the $\vec{V} \times \vec{B}$ field is indicated for comparison with (a)

$$\hat{e}_1 = \cos \theta \cos \phi \hat{x} + \cos \theta \sin \phi \hat{y} - \sin \theta \hat{z} \quad (5)$$

$$\hat{e}_2 = -\sin \phi \hat{x} + \cos \phi \hat{y} \quad (5)$$

$$\hat{e}_3 = \sin \theta \cos \phi \hat{x} + \sin \theta \sin \phi \hat{y} + \cos \theta \hat{z}$$

Since $\vec{E} \cdot \vec{B} = 0$, \vec{E} can be represented by

$$\vec{E} = a_1 \hat{e}_1 + a_2 \hat{e}_2$$

Transforming to spacecraft coordinates, we have

$$\vec{E} = (a_1 \cos \theta \cos \phi - a_2 \sin \phi) \hat{x} + (a_1 \cos \theta \sin \phi + a_2 \cos \phi) \hat{y} - a_1 \sin \theta \hat{z}$$

In regions of slowly changing electric fields, E_x and E_z are measured directly at times of maximum or minimum values of ϕ_m . These measured values may be used to compute a_1 and a_2

$$\begin{aligned} a_1 &= -E_z \csc \theta \\ a_2 &= -(E_z \cos \theta \cos \phi + E_x \csc \phi) \end{aligned} \quad (6)$$

We note that unless $\phi = 0^\circ$ or 180° :

- (1) \vec{E}_p and \vec{B}_p are not orthogonal vectors.
- (2) The y component of the electric field can be computed

$$E_y = -(E_x \cos \phi + E_z \cot \theta) \csc \phi \quad (7)$$

Rearranging terms in Eq. (7), we obtain

$$E_x = -(E_z \cot \theta \sec \phi - E_y \tan \phi) \quad (8)$$

It is useful to define an angle $\Psi = \tan^{-1}(E_x/E_z)$ such that at the angle Ψ , ϕ_E has a maximum value. Since

$$\Psi = \tan^{-1} \left[-\cot \theta \sec \phi - \frac{E_y}{E_z} \tan \phi \right] \quad (9)$$

we can examine its sensitivity to variations in the ratio E_y/E_z . A plot of Ψ as a function of E_y/E_z is given in Figure 3. Magnetic conditions are those of 60600 UT on orbit 517. There are two families of solutions, depending on the size of E_z , which for a given E_y/E_z ratio are separated by 180° . To a zero order approximation, the satellite is moving in the magnetic north-south direction and the spin axis is in the magnetic east-west direction. Because auroral forms tend to be aligned in the magnetic east-west direction, variations of physical quantities along the trajectory should be much greater than their variations in the Y direction, that is, $\partial/\partial y \sim 0$. Since $\nabla \times \vec{E} = 0$ for quasi dc fields, it follows that $(\partial E_y/\partial x) \sim 0$, that is, the Y component of the electric field should be relatively constant. In the evening sector of the northern auroral zone, the electric field is generally toward the magnetic north ($E_x > 0$) and west ($E_y > 0$). From the inclination of magnetic field lines and the condition $\vec{E} \cdot \vec{B} = 0$, it can be shown that $E_z > 0$. We note that along the $E_z > 0$ curve, Ψ only changes from 72° to 81° as the ratio E_y/E_z varies from 0 to 20. This implies that over a wide range of (E_y/E_z) ratios $\Psi \sim \text{constant}$. Thus variations in the electric field perpendicular to \vec{B} can only produce a change in magnitude of ϕ_m or a jump of $\sim 180^\circ$ if E_x (and necessarily E_z) reverse sign.

The main features of this analysis are verified in the data given in Figure 2. The time separation between maxima and minima in ϕ_E are approximately constant prior to 60645 UT. The maximum at ~ 60690 UT is at the appropriate time for $\Psi = \text{const}$. There is an abrupt shift of 180° in the phase of the measured signal at 60710 UT indicating that the ambient electric field changed directions. A calibrate sequence began at 60720 UT. When the data collection resumed, the measured signal indicated that the electric field had a southward component. The reversal at 60710 UT marks the boundary between the auroral oval and the polar cap. In the period 60645 UT to 60690 UT, we assumed that Ψ had the same value that it had before and after this interval. Although in principle the amplitude could be fit to arbitrarily small portions of sine waves, 5-sec periods were chosen to ensure that ϕ_E would be near its maximum or minimum value during a portion of each fit period. As indicated above, further evaluation of the calculated electric fields requires supporting information from other instruments.

2.2 Magnetic Field

The magnetic field is measured by a triaxial fluxgate magnetometer with 3 inductors mounted mutually perpendicular to an accuracy of 0.01° . In-flight, the magnetometer is mounted at the end of an Astromast boom, 6.1 m from the spacecraft body in the spacecraft's spin plane. Nominally, one axis of the magnetometer sensor is parallel to the satellite's spin axis and the other two axes are in the spin plane and parallel to the other two axes of the spacecraft body. The actual orientation of the magnetometer system with respect to the spacecraft axes is determined

by in-flight calibration. The Astromast boom consists of 3 fiberglass longerons in the form of a triple helix. Due to thermal expansion and contraction of the boom, the orientation of the magnetometer system with respect to the spacecraft will vary during an orbit by as much as $\pm 1/4^\circ$. As part of the data reduction procedure, the orientation direction of the magnetometer along the spin axis as a function of time is determined to an accuracy of 0.01° .

Each axis of the magnetometer has a range of $\pm 600 \gamma$ and is read out in steps of 5γ . In order to measure large magnetic fields, there is a neutralization winding about each axis of the magnetometer through which fixed current levels are applied by an automatic ranging current source. Each increment of current is equivalent to a 1000γ offset in the magnetic field. There are 128 increments or steps of current that can be applied, allowing for a dynamic range of $+63,600 \gamma$ to $-64,600 \gamma$ for each axis.

The fluxgate magnetometer outputs are sampled 32 times per second. The offset current is read out in 8 coarse steps, each equivalent to $16,000 \gamma$. The coarse steps are subdivided into 16 fine steps, each equivalent to $1,000 \gamma$. The level of the fine offset current step is sampled by the telemetry stream 16 times per second. The level of the coarse offset current step is sampled by the telemetry stream twice per second.

Because the satellite is spinning with a period of ~ 20 seconds, the magnetic field components in the spin plane of the satellite can change by as much as $15,000 \gamma$ per second. Due to several effects, it is difficult to obtain good measurements under such conditions. First, there is a finite delay between the time when a change in the offset current is made and when the magnetometer has fully responded to the new offset current. Also, when the offset current step is changed, there is some confusion about the appropriate step level for the magnetometer reading since the offset levels are sampled less frequently than the magnetometer. When the magnetic field is changing at a rate of $8,000 \gamma$ per second or less, these problems are solved by discarding the first two magnetometer readings and the last reading at each step level. When the rate is between $8,000 \gamma$ and $15,000 \gamma$ per second, only the first and last magnetometer readings at each step level are discarded. This increases the number of readings used, but it also increases the possibility of obtaining bad readings of the magnetometer. This problem is minimized by comparing the size of the change in the magnetometer readings with the sign of the change in the offset levels for incompatibility and by applying a filter later in the data analysis procedure.

The IGRF-1975 model field, updated to the epoch of the observation, is subtracted from the observed value of the magnetic field. This involves several transformations. The IGRF model, which is given in geodetic coordinates, is first transformed to geographic coordinates, then to earth centered inertial coordinates,

then to satellite coordinates, and finally to magnetometer coordinates. The transformation to magnetometer coordinates nominally consists of a rotation of 3.6° about the spacecraft Z axis and -1.5° about the spacecraft X axis. The actual rotation from spacecraft to magnetometer coordinates must be found for each segment of data due to the twisting and bending of the magnetometer's boom and to uncertainties in the measured spacecraft altitude. This is done by varying the orientation angles by small amounts until the spin axis component of the difference between the model and measured field has a minimal sinusoidal component. If the difference between the model and the true magnetic field is small ($\leq 100 \gamma$), then a complete removal of the sinusoid in the spin axis component of the difference can be obtained. If the difference between the model and the true magnetic field in the spin plane is large ($> 100 \gamma$), the sinusoid in the spin axis component of the difference can only be minimized. The final result is that two of the three magnetometer orientation angles are known to an accuracy of 0.01° . The angle about the spacecraft Z axis varies from 3.3° to 3.9° with a maximum rate of change of $0.02^\circ/\text{minute}$ after sunrise or sunset. The angle about the spacecraft X axis varies from -1.4° to -1.6° .

After the model field has been subtracted from the measured field, the difference (ΔB) may be plotted in magnetometer coordinates or in geodetic coordinates. If ΔB is plotted in magnetometer coordinates, only valid measurements of the components are plotted with straight lines between points. To guard against the use of measurements that contain transients, measurements of ΔB components along each axis which are 400γ greater than the average of the last three valid measurements along that axis are rejected. If ΔB is plotted in geodetic coordinates, invalid measurements of ΔB components are replaced with the last valid measurement and then the ΔB vector is rotated back through the inverse transformation that was used for model field. As a result of the construction of ΔB vectors, the plot of ΔB in geodetic coordinates contains slightly more noise than the plot of ΔB in magnetometer coordinates and contains a sinusoidal error due to the uncertainty in the third magnetometer orientation angle.

2.3 Energetic Electron Spectrometer

Electrons with energies between 0.08 and 17 keV are measured by a parallel plate electrostatic analyzer (Figure 4). This instrument produces a 32 point spectrum once per sec with $\Delta E/E = 0.419$. The geometric factor is $4.68 \times 10^{-5} \text{ cm}^2 \text{ ster}$. The aperture of the instrument is mounted in the spin plane of the satellite. Since the satellite spin period is 20 sec, each spectrum corresponds to approximately an 18° sample in electron pitch angle. In their reduced form, data are available as number flux, energy flux, and average energy as functions of

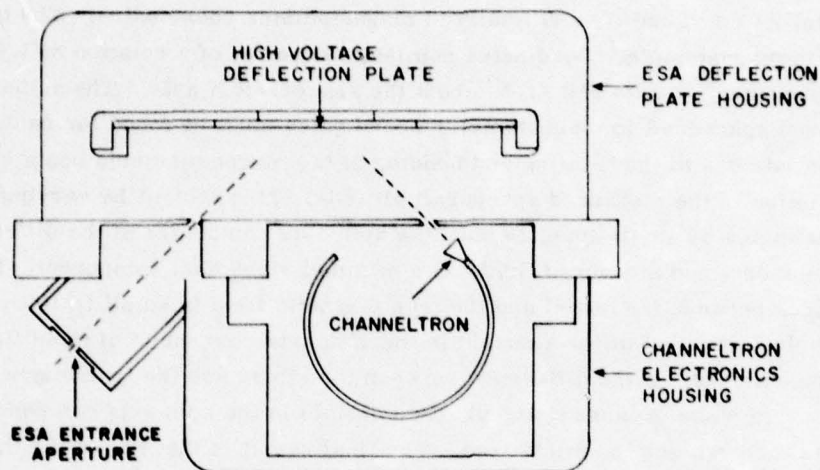


Figure 4. Energetic Electron Spectrometer. Electrons of appropriate energy entering the aperture are deflected by a single high voltage plate into channeltron

universal time, pitch angle, and other standard geophysical coordinates. Individual spectra are also available for detailed analysis of particular auroral events. A more detailed description of the instrument is given by Morel et al.⁵

In the analysis of data from this instrument, two difficulties are apparent. First, due to the relatively small geometric factor of the detector, counting rates produced by diffuse auroral electrons and electrons in the suprathermal tail of auroral spectra are often at or below the level of one count per accumulation interval. Second, the instrument has a single aperture which rotates with the satellite. This often results in the instrument not measuring the most interesting portion of the pitch angle distribution during particular auroral events. For example, the satellite can pass over such features as inverted -V structures in times < 20 seconds. It is thus possible to miss the field-aligned component of the precipitating electron distribution.

5. Morel, P.R., Hanser, F.A., and Sellers, B. (1975) Design Fabrication and Integration of an Electrostatic Analyzer for a Satellite Payload, AFCRI-TR-75-0017.

2.4 Ion Drift Meter

The ion drift-meter experiment consists of two arrays of four passive thermal-ion sensors, each with a circular aperture of 6.8 cm^2 area.⁶ The external configurations of the two arrays, illustrated in Figure 5a, are identical. They are embedded in the surface of the vehicle at diametrically opposite positions. The internal geometry of sensors 1, 2, 3 and 4 is planar. To minimize their response to solar UV the internal geometry of sensors 5, 6, 7 and 8 are nonplanar.⁷ Normal vectors to the apertures of sensors 2 (6) and 4 (8) lie in the spin plane of the satellite at relative look angles of 40° . Sensors 1 (5) and 3 (7) are coplanar with 2 (6) but look out of the spin plane by angles of 40° toward and away from the spin axis, respectively. Using precise satellite attitude information, one observes that the currents measured by sensors 2 (6) and 4 (8) can, in principle, be used to calculate the component of plasma drift in the spin plane, that is, the up-down component of plasma motion normal to the satellite velocity \vec{V}_s . Currents measured by sensors 1 (5) and 3 (7) give the components of plasma drift along the satellite spin axis. Since the satellite motion is primarily north-south, the drift component is nearly east-west. However, the internal design of sensors 5, 6, 7 and 8 has led to uncertainties about the absolute sensitivity to ions of different masses and energies.⁸ This, for the present data set east-west plasma drifts are obtained only from sensors 1 and 3. An example of these results may be found in Appendix A. Besides the plasma drift motion which requires the currents to two sensors, information about the plasma density and the dominant ion species may be gained from the measurements made by individual sensors. The latter, semiquantitative measurement, makes use of the fact that for typical ionic temperatures of $\sim 10^{30} \text{ K}$ the Mach number of the satellite is ~ 1 in a region of H^+ and ~ 5 in an O^+ . Although the currents measured by a sensor, say 2, when facing toward the satellite velocity (ram direction) are comparable for H^+ or O^+ at a given density, the currents measured in the antiram direction are very different. The ratio of currents measured in the ram and antiram directions is much greater in the O^+ than in H^+ regions. In Figure 8a we have plotted the current measured by sensor 2 during part of Rev 517. The maximum currents are measured when the satellite faces in the ram direction and the minimum currents in the antiram directions. At $\sim 60690 \text{ UT}$ the current when facing the antiram direction decreased from

6. Rich, F.J., and Wildman, P.J.L. (1977) A Model for the Electrical Current Collected by a Planar Aperture Ion Collected with a Partially Blocked Field of View, AFGL-TR-770096.
7. Wildman, P.J.L. (1976) Studies of Low-energy Plasma Motion: Results and a New Technique, AFGL-TR-76-0168.
8. Wildman, P.J.L. (1977) A low energy ion sensor for space measurements with reduced photosensitivity, Sp. Sci. Inst. 3:363.

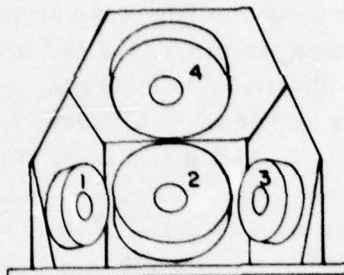


Figure 5a. External Configuration of the Ion Drift Meter Experiments. The surface normal for sensors 2 (6) and 4 (8) lie in the spin plane of the satellite. Sensors 1 (5) and 3 (7) are coplanar with sensor 2 (6) but look out of the spin plane by an angle of 40° toward the - and +Y directions, respectively

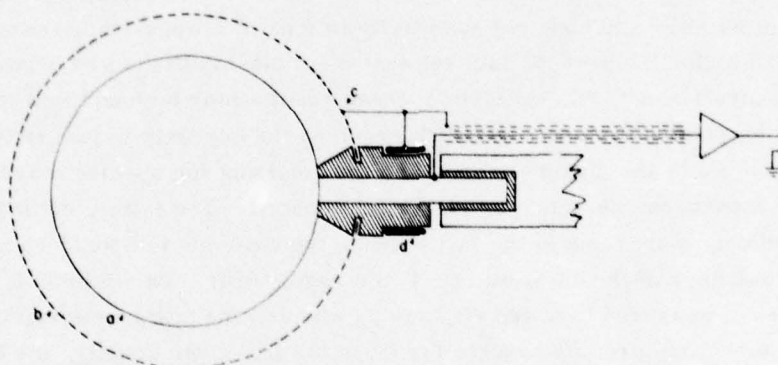


Figure 5b. Schematic of Boom-mounted, Thermal Electron Probe: (a) 2.54 cm radius collector is held at +50 V relative to outer grid; (b) 3.3 cm radius grid of 66.4 percent transparency; (c) electrical connection to drive +8 V to -8 V sweep of grid; (d) guard ring electrically connected to grid

5×10^{-11} A to below the sensors' lower limit of sensitivity. This transition is interpreted as marking the latitudinal boundary between the regions of H^+ and O^+ dominance. At altitudes near 1000 km, this transition usually marks the ionospheric projection of the plasmopause.⁹

9. Taylor, H.A. (1972) The light ion trough, Planet. Space Sci. 20:1953.

2.5 Thermal Electron

The thermal electron sensor (Figure 5b) is a grided, spherical Langmuir probe mounted at the end of a 1.2-m boom projecting parallel to the satellite's spin axis. The probe itself consists of a solid collector of 2.54-cm radius surrounded by a concentric wire mesh grid of 3.30-cm radius and 66.4 percent transparency. The experiment operates in a two-mode, repetitive cycle of 32- or 16-sec duration, depending on command from ground. In the first mode, the grid is held for 29.5 or 13.5 sec at +1.5 V relative to the satellite ground potential. The purpose of the +1.5 V bias is to offset anticipated negative satellite potentials relative to the ambient plasma. In the second mode of operation, the grid is swept from +8 to -8 V in 2.5 sec. Two fixed calibration currents, each of 1-sec duration, are fed into the amplifier every 512 sec. The collector is always held at +50 V relative to the applied grid potential. Thus, any thermal electrons passing through the wire mesh grid are accelerated to the collector. The density and temperature of the ambient electrons, as well as the potential of the spacecraft ground relative to the plasma, are determined from the measured electron current versus applied voltage relationship. The analysis is based on standard Langmuir probe theory and uses the function fitting method of Fletcher and Powell.¹⁰ The data rate is 16 samples per sec. Most of the physical information is contained in the 6 to 15 samples nearest the voltage where the probe potential equals the plasma potential. During the fixed voltage mode, electron densities are calculated from the electron currents using the electron temperature and satellite potential measured during the previous swept voltage mode period. This method of normalizing fixed voltage mode data assumes that the electron temperature and satellite potential are unchanged for the 29-sec duration of the fixed voltage mode. This assumption breaks down in the auroral zone where energetic charged particles cause frequent and rapid fluctuations of the satellite potential. A fluctuation in the satellite potential with respect to the plasma causes changes in the measured electron currents similar to changes produced by density variations. Satellite potential fluctuations may be distinguished from density fluctuations by referring to simultaneous measurements by the ion drift meter. Changes in the plasma density produce similar variations in the electron and ion sensor currents. Negative excursions of the satellite potentials reduce the currents to the thermal electron sensor, but leave the ion sensor measurements virtually unchanged. Positive excursions of the satellite potentials reduce the thermal ion current and increase the thermal electron current.

10. Fletcher, R., Powell, M.J.D. (1964) A rapidly convergent descent method for minimization, Computer Journal 6:163.

3. OBSERVATIONAL RESULTS FOR CASE STUDY

In this section, data from the various experiments on S3-2 are presented from a single pass of the late evening sector of the northern auroral zone. The purpose of this exercise is to show how correlated measurements may be used to investigate some electrodynamic properties of aurorae. The one pass over the auroral zone (orbit 517) was chosen because of the availability of nearly simultaneous auroral imagery from a DMSP satellite. Structurally, this section consists of four parts. The first subsection provides an overview of the S3-2/DMSP observations; the measurements are presented as functions of universal time in seconds of the day. Based on the overview, the auroral zone is divided into three phenomenologically distinct regions. Characteristics of each region are studied in detail in the three following subsections. Region 1 corresponds to diffuse aurora (encountered prior to 60646 UT of orbit 517). It is characterized by relatively soft electron precipitation and by complex field-aligned currents superimposed on a general background of current into the ionosphere. Region 2 (encountered from 60646 UT to 60653 UT) corresponds to an intense return current for an auroral arc. The current is carried by cold electrons drifting along magnetic field lines at speeds approximating conditions that are critical for the onset of ion cyclotron turbulence. In this region there is also evidence for an electric field component along \vec{B} . Region 3 (encountered from 60653 UT to 606700 UT) corresponds to the region of the discrete aurorae. Special attention is directed to the relationship between convective electric fields and precipitating electrons.

Before considering the actual data, one finds it useful to summarize briefly the general features of expected observation for a satellite at an altitude of 1200 km in the late evening sector as it moves from mid-latitude across the auroral zone into the polar cap. These features are based on many previously reported satellite measurements.

1. Thermal Plasma. As the satellite crosses the ionospheric projection of the plasmapause, the plasma density decreases. It remains low across the region of the trough and diffuse aurorae. It rises sharply in the region of discrete aurorae where plasma is produced by precipitating keV electrons.

2. Energetic Electrons. In the region of the diffuse aurorae, relatively uniform, quasi-isotropic fluxes of electrons with $E \leq 1$ keV are generally encountered. Over the region of discrete aurorae, electron fluxes are quite variable in energy, pitch angle, and intensity. Characteristic energies may exceed 10 keV in this region.

3. Electric Fields. In the evening sector the auroral electrojet is generally directed toward the east. Since the Hall conductivity is greater than the Pedersen conductivity at the altitude of the electrojet and since the current is carried by

electrons, the electric field should have a northward orientation. To cause an equatorward component of plasma drift in this region, E generally has a small (≤ 10 mV/m) westward component. In the polar cap the electric field has a dawn to dusk orientation.

4. Magnetic Fields. In the evening sector the region of diffuse aurorae is one of current into the ionosphere, while in the region of discrete aurorae the current (which is carried by precipitating electrons) is out of the ionosphere. The satellite can thus be expected to measure a growing eastward perturbation as it moves across the diffuse aurorae. The eastward component should decrease as the satellite crosses the discrete arc region.

3.1 Overview

Part of the DMSP imagery taken at northern high latitudes on 11 January 1976 is given in Figure 6. The superimposed grids give the corrected geomagnetic longitude and latitude projected to an altitude of 100 km. The trajectory of S3-2 orbit, also projected in corrected geomagnetic longitude and latitude to 100 km, is represented by the dashed line. The temporal separation between the DMSP and S3-2 trajectory crossover in this coordinate system was ~ 14 min. Measurements of S3-2 were after those of DMSP. We note that auroral forms tend to be stationary in earth-centered inertial systems, but geomagnetic coordinates rotate with the earth. In the 14 min between the DMSP and S3-2 crossover, the earth rotated under the arc $\sim 3.5^\circ$ in longitude. Thus, relative to the arc, the S3-2 orbit should be moved 3.5° to the east; that is, away from the folded arc and well into the straight line arc segment. This arc is tilted by $\sim 15^\circ$ away from the magnetic east-west direction. The S3-2 trajectory crossed the arc at an angle of $\sim 30^\circ$ away from normal incidence.

It appears that the auroral form remained relatively stationary during the 14 min between the DMSP and S3-2 crossovers. Evidence supporting this conclusion is found in Figure 7 where we have plotted AE as well as the H, Z and D components of the magnetic field measured at Dixon Island. The position of Dixon Island is marked by the symbol x on Figure 6. The AE index indicates that the passes of both satellites correspond to the beginning of a substorm recovery phase. This is supported by the DMSP imagery which shows a disordered region near local midnight. Although such periods normally involve large temporal variations in auroral behavior, the S3-2 orbit lies to the west of the active region. The Dixon Island magnetogram is relatively constant in all three components during the 10-min period. Since Dixon Island is magnetically due north of where S3-2 crossed the auroral oval, the constant magnetic field at this station is consistent with stable auroral features.



Figure 6. DMSP Imagery for an Auroral Form Taken ~ 14 min Prior to S3-2 Overpass (dashed line). The superimposed grid gives the geomagnetic latitude and longitude at an altitude of 100 km. The position of Dixon Island is marked by the symbol x

The relative constancy of the auroral features is supported by the high degree of consistency between S3-2 particle measurements and the DMSP imagery. As discussed below, an inverted-V event¹¹ was observed in the energetic electron measurement beginning at 60653 UT. Tracing magnetic field lines from the altitude of S3-2 to 100 km, and allowing for earth-rotational effects, we find that this coincides with the equatorward boundary of the discrete auroral arc shown in Figure 6.

A summary of plasma and field conditions encountered during orbit 517 is given in Figures 8, 9 and 10. Going from the top to bottom panels of Figure 8, we have plotted as functions of universal time, altitude, invariant latitude (Λ) and magnetic local time: (a) I_2 the current measured by the ion drift meter sensor 2, (b) N_i the total ion density, (c) E the spin-plane component of the electric field, and (d) the directional electron flux.

11. Ackerson, K. L., and Franck, L. A. (1972) Correlated satellite measurements of low energy electron precipitation and ground based observations of a visible auroral arc, J. Geophys. Res. 77:1128.

AE INDEX & DIXON ISLAND MAGNETOGRAM

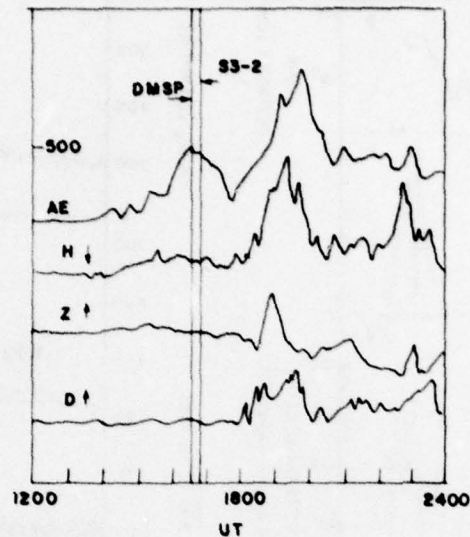


Figure 7. Auroral Electrojet (AE) Index and Dixon Island Magnetogram Components for 11 January 1976. The times at which DMSP and S3-2 passed over the auroral are indicated

Considering first the ion drift meter data (Figure 8a, b), we note several significant points.

- (1) There is a latitudinal transition from a region of H^+ to O^+ dominance starting at $\Lambda = 59.2^\circ$ (60590 UT). This is seen as a dramatic change in the ratio of the current measured as the sensor faces the ram and antiram directions, as discussed previously.
- (2) The ion density decreased from $\sim 10^3 \text{ cm}^{-3}$ at $\Lambda = 51^\circ$ to a trough minimum of $3 \times 10^2 \text{ cm}^{-3}$ at $\Lambda = 55.5$.
- (3) A local density maximum at $\Lambda = 57.5^\circ$ is followed by a significant density increase as the satellite moved poleward into the region of O^+ dominance. A second high latitude trough is found at $\sim 60700 \text{ UT}$ as the satellite passed from the auroral oval to the polar cap.

The electric field measurements given in Figure 8c are 5-sec averages based on the fitted potentials given in the bottom panel of Figure 2. Smaller time-scale residues are, for the time being, ignored; E is the projection of the total electric field into the spin plane of the satellite. Unless explicitly stated otherwise, E is assumed to be perpendicular to \vec{B} . At this time the satellite was moving $\sim 15^\circ$ to the west of magnetic north. Thus, the positive values of the component along the

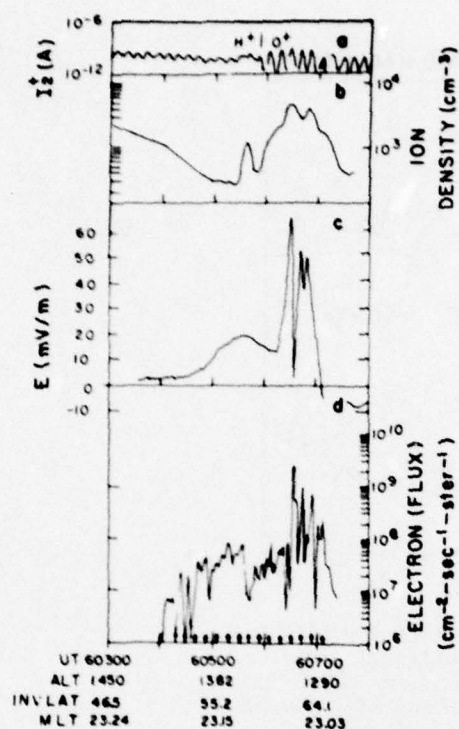


Figure 8. Simultaneous Measurements of (a) Current to Ion Sensor 2; (b) Ion Density; (c) 5-sec Averaged Values of the Electric Field; and (d) Directional Electron Flux. The arrows at the bottom of the plot indicate times when the energetic electron spectrometer was looking upward along magnetic field lines

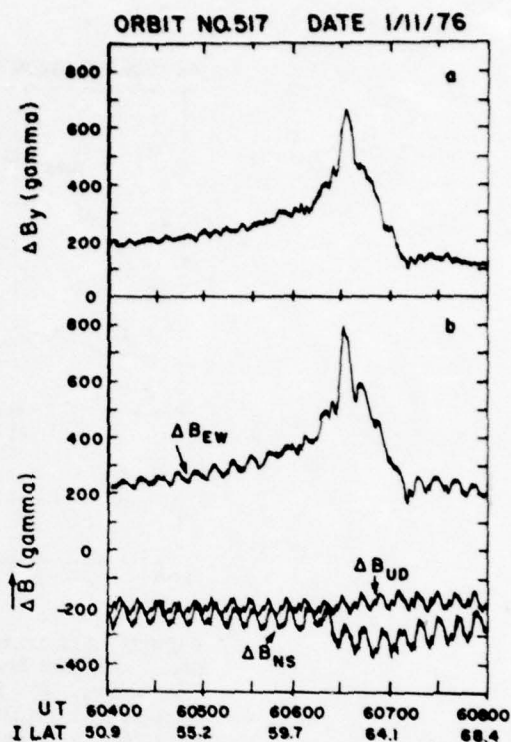


Figure 9. Differences Between Measured Magnetic Field Components and the Corresponding IGRF Values: (a) Spin Axis Component in Magnetometer Coordinates; (b) North-South, East-West and Up-down Components in Geocentric Coordinates

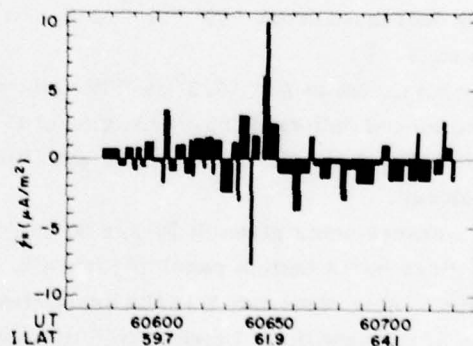


Figure 10. Current Densities Calculated from Variations of ΔB_γ (Figure 9a). Positive currents are parallel to \mathbf{B} . In the northern hemisphere they are into the ionosphere

trajectory indicate that E is approximately in the magnetic northward direction. The plasma drift caused by this component is approximately in the magnetic westward direction. The electric field rose from a level of <2 mV/m at $\Lambda = 54^\circ$ to a first maximum of 20 mV/m at 57° . It decreased to 14 mV/m before rising to a maximum of 66 mV/m at $\Lambda = 61.9^\circ$. As the satellite crossed the position of the discrete arc, E decreased to an average value of 0.5 mV/m. It showed rapid variations, then reversed sign (developed a southward component) as the satellite passed into the polar cap.

The energetic electron flux rose above the instrument background level at approximately the same time that the electric field began to increase. This flux reached a maximum value of 8×10^7 (cm² sec ster)⁻¹ at 60560 UT then decreased abruptly. The satellite then passed through a series of rapid flux variations between 7×10^7 (cm sec ster)⁻¹ and the instrument background level. These fluctuations are due to satellite induced spin modulations and spatial-temporal variations of the electron flux. At 60653 UT the flux increased abruptly to 3×10^9 (cm²-sec-ster)⁻¹. Several local maxima were measured up to 60720 UT when the flux fell below the instrument background level.

Components of the magnetic field after subtraction of the model field are plotted as functions of universal time in Figure 9a, b, respectively, in magnetometer and geodetic coordinates; ΔB_y is the spin-axis components in the satellite coordinate system. At the beginning of the data stream in Figure 9a, there is a 10 γ amplitude periodic signal due to an imperfect transformation of the model field into magnetometer coordinates. Prior to 60570 UT, there is a steadily increasing difference between the measured and model spin-axis component. This is due partially to a systematic error in the model field and partially to a field-aligned current into the ionosphere with an intensity $<0.1 \mu A/M^2$.

The magnetometer data naturally divide into three periods of contrasting behavior. In the first period, between 60570 UT and 606046 UT, the slope of ΔB_y is generally positive with brief periods of negative slope interspersed. It is important to note that the alternating periods of negative and positive slope do not correlate with the satellite spin period. This suggests that they result from currents into and out of the ionosphere. In the second period, between 606046 UT and 60653 UT, ΔB_y increased rapidly to a maximum of 670 γ . This is 310 γ higher than the value of 60570 UT. The third period, after 60653 UT, is characterized by a negative slope with brief periods of positive slope embedded.

The differences between the three measured and model field components in geodetic coordinates are given as north-south (NS), east-west (EW), and up-down (UD). The deflections are positive toward north, east, and down, respectively. There is an ~ 80 γ oscillation in the NS and UD components and a 40 γ oscillation in the EW component. These derive from uncertainties concerning the magnetometer

calibration and its precise orientation in the spin plane. The increased amplitude of the EW signal results from folding spin-plane information into the spin axis measurements. The main features of ΔB_y are reproduced in ΔB_{EW} . However, the maximum deflection at 60653 UT is $\sim 500 \gamma$ above the component's value at 60570 UT. The mean value of the vertical component maintained a constant value of approximately -250γ throughout the period of study. The NS component has a mean value of -250γ to 60640 UT when it decreased by about -50γ . This component then slowly returned to its initial value. These variations suggest that deflections prior to 60640 UT were mainly in the east-west directions. In the region of the auroral arc, the magnetic deflection was toward south of east. This measurement is consistent with the DMSP imagery which shows that the arc was tilted by $\sim 15^\circ$ away from the magnetic east-west direction. If the current sheets were parallel to the arc, a south of east total magnetic deflection should be observed. It should also be noted that an eastward electrojet due to a Hall current in the lower ionosphere would also produce a southward deflection. Without other information, it is not possible to determine the relative contributions of the electrojet and the field-aligned currents to the southward component of the deflection. At a satellite altitude of 1300 km, it is expected that the electrojet contribution would not be large.¹²

In order to avoid ambiguities resulting from the spin-induced oscillation in the geodetic EW component, we have used the spin axis data to calculate values of $j_{||}$ given in Figure 10. The currents are positive if they are directed into (along B) the ionosphere. The current density calculations are done using the infinite current sheet approximation to Maxwell's equation:

$$j_{||} = \frac{1}{(\mu_0 V_s)} \frac{\partial \Delta B_y}{\partial t} \quad (10)$$

Our use of magnetometer coordinates implies that the calculated $j_{||}$ magnitudes, at least near the auroral arc, are lower bounds on the true values. This can be seen from the fact that the deflections between 60570 UT and 60653 UT were $\Delta B_y \sim 320 \gamma$ and $\Delta B_{EW} \sim 500 \gamma$ in spacecraft and geodetic coordinates, respectively. Current densities are also underestimated due to the fact that the satellite trajectory is at an angle ζ away from normal incidence. For an infinite current sheet $j_{||} = \mu_0 \partial \Delta B_{EW} / \partial x$. The measured quantity is $\partial \Delta B_{EW} / \partial s = \mu_0 j_{||} \cos \zeta$, the variations of the Y component along the satellite trajectory. In the case of orbit 517, the DMSP imagery shows that $\zeta \simeq 30^\circ$. Thus, the current densities reported

12. Langel, R.A. (1975) A comparison of electric and magnetic field data from the OGO 6 spacecraft, J. Geophys. Res. 80:4661.

here may be too small by a factor of 2 in the vicinity of the auroral arc. However, the sign, location and relative magnitudes of the current sheets are accurate.

In the following three subsections we consider, in detail, the three regions identified in the magnetometer measurements. Special emphasis is placed on comparisons between the high-time resolution measurements of the various instruments. Physical implications of the measurements are examined only insofar as they help understand the measurements of other instruments; for example, when the $\vec{E} \cdot \vec{B} = 0$ condition is not valid.

3.2 Region 1

This region is encountered between $\Lambda = 54.8^\circ$ (60490 UT) and $\Lambda = 61.7^\circ$ (60646 UT). It extends from the ionospheric projection of the plasmopause across the region of the diffuse aurorae. The plasmopause projection and the ionospheric trough are at latitudes that are equatorward of their quiet time values ($\Lambda \geq 60^\circ$). This equatorward displacement was probably not due to the ongoing minor sub-storm but to the result of the severe magnetic activity that marked the last 6 hours of 10 January and the first 3 hours of 11 January. During these periods, K_p had values of 7, 7 and 7⁺. Under such conditions, intense convective electric fields increase ionospheric recombination rates¹³ and cause plasmaspheric particles to drift beyond the magnetopause.¹⁴ Thus, the plasmopause moves earthward and the trough moves equatorward.

The region of the diffuse aurorae maps into the central portion of the plasma-sheet. It is generally characterized by relatively uniform fluxes of protons and electrons of comparable intensity.¹⁵ In the evening sector, this region has been shown by previous satellite studies to be one of field-aligned currents into the ionosphere.¹⁶ Data presented in Figure 9a show that in this region ΔB_y generally had positive slope, indicating the presence of field-aligned currents into the ionosphere. There are, however, brief periods in which the slope of ΔB_y was negative. In the remainder of this subsection, high-time resolution data are examined to

-
13. Schunk, R.W., Raitt, W.J., and Banks, P.M. (1975) Effect of electric fields on the daytime high latitude E and F regions, *J. Geophys. Res.* 80:3121.
 14. Chappell, C.R., Harris, K.K., and Sharp, G.W. (1970) A study of the influence of magnetic activity on the location of the plasmopause as measured by OGO 5, *J. Geophys. Res.* 75:50.
 15. Lui, A.T.Y., Venkatesan, D., Anger, C.D., Akasofu, S.-I., Heikkila, W.J., Winningham, J.D., and Burrows, J.R. (1977) Simultaneous observations of particle precipitation and auroral emissions by the ISIS 2 satellite in the 19-24 MLT sector, *J. Geophys. Res.* 82:2210.
 16. Hjima, T., and Potemera, T.A. (1978) Large-scale characteristics of field-aligned currents associated with substorms, *J. Geophys. Res.* 83:599.

show that these result from the satellite passing through field-aligned current sheets rather than from defects of the data reduction process.

Expanded plots of ΔB_y , the current measured by the thermal electron probe and the energetic electron flux, are given in Figure 11. Arrows at the bottom of the figure indicate times when the electron spectrometer was looking up or down magnetic field lines. Currents into (out of) the ionosphere are characterized by increasing (decreasing) ΔB_y . There are at least four periods, marked at the top of the figure, during which ΔB_y decreased. During each of these events, the thermal electron current decreased by approximately an order of magnitude. Since the ion densities showed no similar fluctuations, we conclude that the thermal electron current decreased because of negative excursions of the satellite potential. Negative satellite potential fluctuations indicate a local enhancement of the energetic electron flux. The negative slope of ΔB_y also indicates that they are also regions of enhanced electron precipitation. It is thus expected that the electron spectrometer would observe increased (decreased) fluxes while looking up (down) magnetic field lines. During events 1 and 3, the spectrometer measured slightly increased fluxes at pitch angles near 90° . At the time of event 4 the flux dropped to instrument background at pitch angles near 180° . These results are consistent with the magnetometer and thermal probe measurements.

During event 2, the spectrometer measured fluxes between approximately 0° and 90° . Here the measured electron flux was decreasing, a result contrary to expectations. It can be reconciled with the magnetometer and thermal probe data if the current carrying electrons had energies outside the spectrometer's range of sensitivity. If the precipitating electrons had more energy than 17 keV, the region would be marked by an enhanced Pedersen conductivity in the lower ionosphere. This would lead to polarization electric fields that would decrease the total electric field component in the north-south direction. No evidence of such a fluctuation in E can be found between 60612 UT and 60616 UT (of Figure 2). The other alternative is that the current was carried by field-aligned electrons with energies less than 100 eV. By what plasma sheet process this could happen is not understood.

To summarize: There is substantial point by point agreement between the magnetometer and the thermal electron probe results. There exist regions of enhanced soft particle precipitation embedded within the part of the ionosphere that maps into the central plasma sheet. These regions are quite narrow having latitudinal widths of ≤ 20 km at altitudes of 1300 km. Similar structures have been previously noted in INJUN 5 data.¹⁷

17. Burke, W.J., Donatelli, D.E., and Sagalyn, R.C. (1978) INJUN 5 observations of low-energy plasma in the high latitude topside ionosphere, J. Geophys. Res. 83:2047.

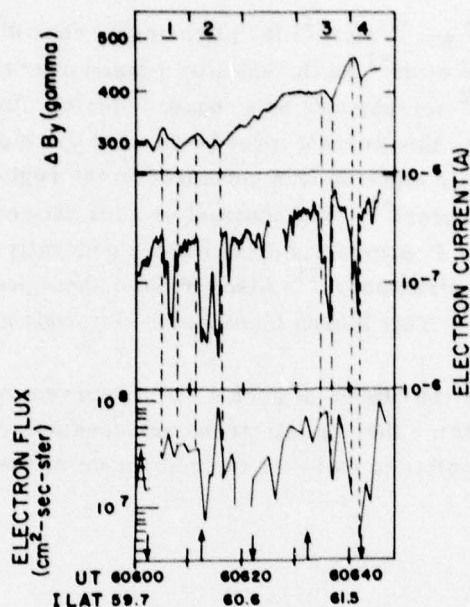


Figure 11. High-time Resolution Measurements of ΔB_y , the Current Measured by the Thermal Electron Probe and the Energetic Electron Directional Flux. Attention is directed to four events during which ΔB_y decreased, indicating a current out of the ionosphere

3.3 Region 2

This region was encountered between 60646 UT ($\Lambda = 61.7$) and 60653 UT ($\Lambda = 62.0^\circ$); it is characterized by intense currents into the ionosphere. The position and orientation of the current sheet suggest that it constitutes the return current of the auroral arc.¹⁸ Attention is directed to the most intense current measured between 60646 UT and 60648 UT. Using Eq. (10), one observes that a lower bound on j_{\parallel} has been set up at $10 \mu\text{A}/\text{m}^2$. The drift meter was looking close to the ram direction. The ion density was $\sim 3 \times 10^3 \text{ cm}^{-3}$. It had a westward drift component (discussed below) but no significant velocity up or down the field line. The thermal electron temperature, measured at 60628 UT was $\sim 3150^\circ\text{K}$. The particle spectrometer measured a local maximum flux of $9 \times 10^7 \text{ (cm}^2 \text{ sec ster)}$ at pitch angles near 90° (60646 UT). The electron flux fell below the instrument's

18. Anderson, H.R., and Vondrak, R.R. (1975) Observations of Birkeland currents at auroral latitudes, Ref. Geophys. Sp. Phys. 13:243.

sensitivity level ($10^7 \text{ cm}^{-2} \text{ sec}^{-1} \text{ ster}^{-1}$) for pitch angles near 0° before rising to a value of $2 \times 10^9 \text{ (cm}^2 \text{ sec ster)}^{-1}$ as the satellite passed over the auroral form.

A current of $10 \mu\text{A/m}^2$ corresponds to a charged particle flux of $6 \times 10^9 \text{ (cm}^2 \text{ sec)}^{-1}$. For the most part, this current must be carried by cold ionospheric electrons since the energetic electron flux measured in the region of the return current was $<10^8 \text{ (cm}^2 \text{ sec ster)}^{-1}$. The thermal protons showed no measurable field-aligned drift motion. Precipitating protons are generally not detected in the vicinity of inverted -V structures.¹¹ Also, plasma sheet proton fluxes are typically $<10^8 \text{ (cm}^2 \text{ sec)}^{-1}$. This leaves ionospheric electrons as the only viable candidates.

We must now consider the effects of such a strong current on the stability of the ionospheric plasma. If the thermal electrons are considered to be the main current carriers, it is possible to estimate the component of their velocity along the magnetic field.

$$V_{e\parallel} = j_{\parallel} / q N_e \quad (11)$$

For $j_{\parallel} \geq 10 \mu\text{A/m}^2$ and $N_e = 3 \times 10^9 \text{ m}^{-3}$, $V_{e\parallel} \geq 20 \text{ km/sec}$. The thermal speed (a_e) of the electrons $\sim 300 \text{ km/sec}$. The ratio $V_{e\parallel}/a_e \geq 0.07$ is approximately equal to the critical value for the onset of 0^+ cyclotron turbulence with $T_e/T_i \sim 3$.¹⁹ This turbulence changes the effective collision frequency ν_{eff} of drifting electrons. The resistivity of the field lines is given by

$$\eta = (\nu_{\text{eff}}/\omega_{pe}) / (\epsilon_0 \omega_{pe}) \quad (12)$$

where ω_{pe} is the electron plasma frequency. In anomalously resistive plasmas experimentally observed values of $\nu_{\text{eff}}/\omega_{pe}$ range between 5.3×10^{-3} and 2.5×10^{-2} .²⁰ Thus η should lie between 200 and 900 ohm-m. Substitution into ohm's law, $E_{\parallel} = \eta j_{\parallel}$ shows that E_{\parallel} should fall between 2 and 9 mV/m. It should be noted that insofar as our calculations of j_{\parallel} is a lower limit, so too is the possible range for E_{\parallel} .

Evidence for the existence of a component of \vec{E} parallel to \vec{B} at $\sim 60647 \text{ UT}$ must now be considered. The ϕ_e measurements (Figure 2) went through a local minimum at 60645 UT then began to increase in a sinusoidal fashion. Between 60647 UT and 60648 UT, ϕ_m abruptly approached the level of $\phi_{v \times b}$. That is, aside

19. Kindel, J. M., and Kennel, C. F. (1971) Topside current instabilities, J. Geophys. Res. 76:3065.

20. Shawhan, S. D., Falthammer, C. G., and Block, L. P. (1978) In the nature of large auroral zone electric fields at $1 R_E$ altitude, J. Geophys. Res. 83:1049.

from the potential due to the satellite motion across magnetic field lines, no potential difference was measured along the dipole. This implies that either \vec{E} went to zero or was perpendicular to the dipole orientation. The first hypothesis is contradicted by the relative currents measured by the drift meter sensors 1 and 3 between 60645 UT and 60650 UT. Figure 12 shows that $I_1 > I_3$ throughout this period. Prior to 60647 UT, the I_1/I_3 ratio was 1.4; it decreased to 1.05 at 60647 UT then returned to a value of 1.4. A calculation in Appendix A shows that E_f decreased from 29.8 mV/m to 8.9 mV/m, then returned to 30.0 mV/m. Since $\vec{E} \neq 0$ it must be oriented perpendicular to the dipole. The orientation of the dipole and the projection of B in the spin plane at 60647 UT is given in Figure 16. Since $E_f = 8.9$ mV/m, a simple trigonometric argument leads to a value of $E_{||} = 10.2$ mV/v. This is slightly higher than the upper range of $E_{||}$ calculated above. If we have underestimated $j_{||}$ by a factor of 2, $E_{||}$ would lie in the middle of the calculated range.

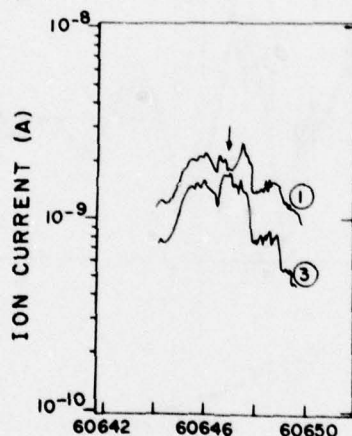


Figure 12. Current Measurements by the Ion Drift Sensors 1 and 3 near 60646 UT. The fact that $I_1 > I_3$ indicates that the plasma has a westward drift component. The arrow indicates the time at which sensors 1, 2 and 3 were facing closest to the ram direction

3.4 Region 3

Region 3 corresponds to that of the auroral form noted in the DMSP imagery (Figure 6). It was encountered by S3-2 beginning of 60653 UT. As mentioned above, magnetic field lines were traced from the altitude of the satellite to that of

the arc. With allowance for the earth's rotation, it was found that the S3-2 position at 60653 UT agreed with that of equatorward boundary of the auroral arc.

Data relevant to an understanding of the electrodynamics of Region 3 are presented in Figures 13 and 14. In Figure 13 we have plotted as functions of universal time and Λ : (a) the potentials measured by the spinning dipole and the quarter-wave sine functions to which they have been fit; (b) the spin axis component of the magnetic field; and (c) the electron directional flux using arrows to indicate times when the sensor was closest to looking up and down magnetic field lines. The electron spectra that were measured approximately every other second are given in Figure 14. The range of pitch angles scanned during the one second of measurements is indicated for reference. The dotted lines indicate the one count per accumulation period flux level. An electron flux at or above this level is indicated by

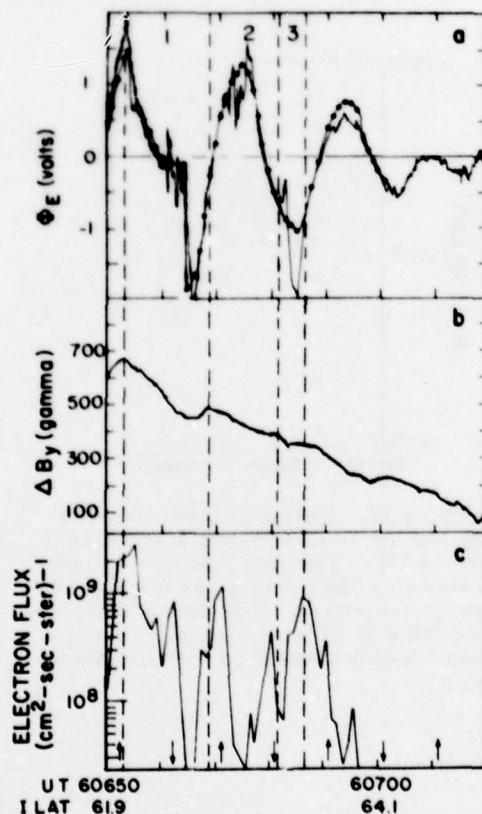


Figure 13. Measurements in Region 3 as Functions of UT and Λ . Plot (a) gives the potential and the fitted function (dotted lines); plot (b) gives ΔB_y and (c) the electron directional flux

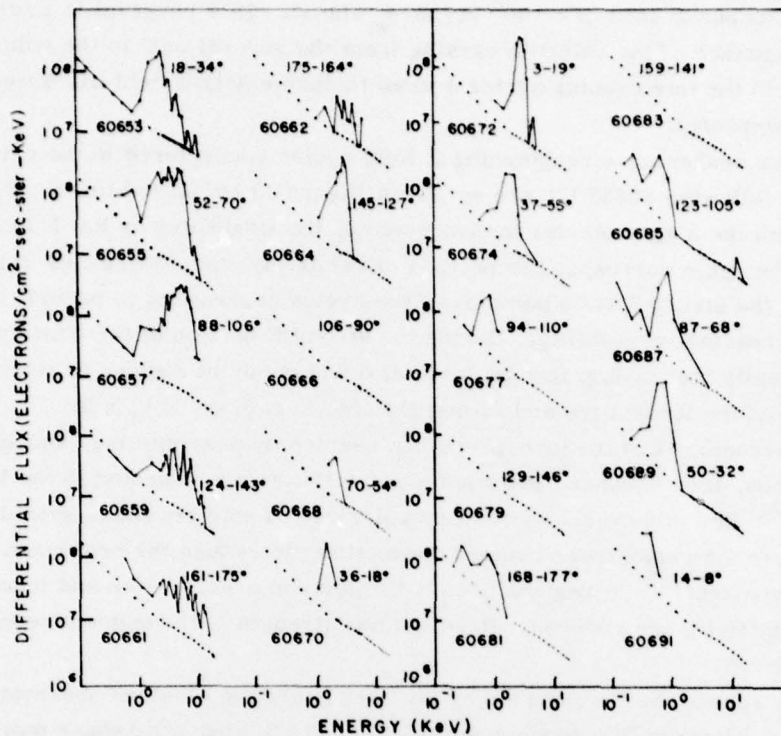


Figure 14. Electron Spectra Measured in Region 3. The range of pitch angles and the UT of the measurements are indicated

a solid line. Because the satellite potential was severely depressed throughout the 60653 UT - 606700 UT time period, no additional information could be gained from the thermal electron probe.

Electric field values given in Figure 8c were quite variable in Region 3. However, these values were calculated using ϕ_{fit} . Variations on time scales less than 5 sec are smoothed by this procedure. Finer time scale resolution may be gained by comparing values of ϕ_e and ϕ_{fit} . Except for 60662 UT when ϕ_e and ϕ_{fit} had opposite signs, the electric field has been underestimated (overestimated) at times when $|\phi_e| < (>) |\phi_{fit}|$. Thus the value of E just prior to entering the arc was $\sim 1/3$ greater than the calculated value of 66 mV/v. The electric field strength decreased rapidly to an average value of 0.5 mV/m. At 60665 UT it increased abruptly to its pre-arc value. Between 60671 and 60676 UT the field weakened, then increased. A third weakening-strengthening cycle is again found between 60682 and 60687 UT. After this time the "northward" electric field component weakened rapidly and reversed sign at 60710 UT. The electric field sign reversed

is evidenced by phase shift of $\sim 180^\circ$ in the Φ_e signal. This reversal is interpreted as the signature of the satellite passing from the auroral oval to the polar cap. We note that in the late evening sector a dawn to dusk electric field has a weak southward component.

The three weakening-strengthening E field cycles encountered in the period immediately following 60653 UT are set off in Figure 13 by dashed lines. When compared with the magnetometer measurements, the weakening or low E field portions of the cycle correspond to periods of relatively steep decreases in ΔB_y . Conversely, the strong E field portions of the cycles correspond to periods when ΔB_y was decreasing very slowly. During the strong E portion of the first cycle, ΔB_y was actually increasing; that is, weak E fields occur in regions of strong currents out of the ionosphere and strong E fields in regions of $j_{\parallel} \geq 0$.

If the currents out of the ionosphere are carried by precipitating, energetic (keV) electrons, then enhanced Pedersen conductivities are expected in the lower ionosphere.²¹ In a steady-state condition polarization electric fields should develop across the regions of enhanced conductivity to reduce the cross-arc electric field component.²² In regions of $j_{\parallel} \geq 0$, electron precipitation and ionospheric conductivity are reduced. Here the full strength of the convective electric field is observed.

This interpretation is supported by the S3-2 energetic electron observations. The maximum electron flux was measured at 60655 UT when the sensor was detecting particles with pitch angles between 52° and 70° . The electron energy distribution appears to be that of an inverted-V event.¹¹ The peak energy of the spectrum shifts to higher values between 60653 and 60657 UT. Significant fluxes of electrons were measured between 60659 and 60664 UT while the sensor was looking down the field lines at mirroring and backscattered electrons. The observation of backscattered keV electrons in a region of decreasing ΔB_y indicates that the precipitating electrons were of the same or greater energies. These electrons are capable of producing visible auroral luminosity and enhanced conductivity. At 60666 UT the electron flux abruptly fell below the level of detectability and remained at a low level until 60671 UT. During this period $\partial \Delta B_y / \partial t \geq 0$ and E briefly went to its highest value.

As the slope of the ΔB_y curve became negative at 60671 UT, E began to decrease and the electron flux increased. The spectrum measured at 60672 UT is narrowly distributed in energy around 4 keV. As the detector moved away from

21. Rees, M.H. (1963) Auroral ionization and excitation by incident energetic electrons, *Planet Sp. Sci.* **11**:1209.

22. Bostrom, R. (1964) A model of auroral electrojets, *J. Geophys. Res.* **69**:4983.

looking up the field line, the measured flux decreased. The fact that ΔB_y and E continued to decrease until 60675 UT suggests that the current was carried by a highly monoenergetic beam of electrons (perhaps accelerated by a double layer parallel electric field at altitudes well above 1300 km).²³ The beginning of the third cycle is marked by a sudden decrease in ΔB_y and a decrease in E. The spectrometer was looking down the magnetic field line but did not detect any back-scattered flux. The increasing E field at 60675 UT when the measured electron flux was increasing, appears to contradict our hypothesis. However, the spectra at this time indicate that most of the electrons had energies less than 1 keV. Most of the ionization produced by these electrons is at altitudes greater than 150 km.²¹ In this case, the integrated conductivity of the ionosphere would remain at a relatively low value.

The S3-2 observations suggest a more complex situation than might be assumed from the DMSP image which showed a single auroral arc. There are several explanations of this apparent difference:

1. Two new arcs developed in the 14 min between the DMSP and S3-2 overpasses.
2. Due to their finite extents in altitude and latitude along slanted magnetic lines, several arcs overlapped in the DMSP image.
3. Only in cycle 1 was the precipitation sufficiently energetic and intense to produce a visual luminosity greater than the 2 kR DMSP lower limit of sensitivity.

The constancy of the Dixon Island magnetogram (Figure 6) makes the first hypothesis seem unlikely. The low energy of the electron flux observed during the third cycle suggests that the third hypothesis may explain the third cycle data but it is a less likely explanation of the second cycle. It seems likely that S3-2 passed over three parallel auroral arcs. The most poleward may have been sub-visual. Due to the slant of the magnetic field lines, the other two parallel arcs could not be resolved in the DMSP image.

4. CONCLUSIONS

In this paper we have given a detailed description of the instrumentation aboard the polar orbiting satellite S3-2 and the ways in which measurements are reduced to give geophysically meaningful quantities. Geophysical information contained in the high temporal resolution data has been illustrated using the measurements of an auroral overpass in the late evening sector when simultaneous DMSP imagery was available. The validity of data reduction processes is

23. Torbert, R.B., and Mozer, F.S. (1978) Electrostatic shocks as the source of discrete auroral arcs, Geophys. Res. Lett. 5:135.

corroborated by detailed comparison of simultaneous measurements of the entire complement of scientific experiments on the S3-2 satellite.

Data presented here suggest that the auroral oval can be divided into three regions. In the region of the diffuse aurorae, very complicated structures of currents into and out of the ionosphere were observed to be superimposed on general trend of current into the ionosphere. Simultaneous depressions of the satellite potential relative to the ambient plasma indicate that the currents are real rather than artifacts of the data reduction process. The second region, characterized by an intense current into the ionosphere, is probably the return current associated with an adjacent auroral form observed by DMSP. The current is carried by cold ionospheric electrons drifting up magnetic field lines at speeds close to that required for the onset of O^+ cyclotron turbulence. Evidence for a localized parallel electric field of ~ 10 mV/m was examined. The third region was that of the auroral form detected by DMSP. Cyclical decreases and increases in the component of the electric field across the arc suggest that S3-2 passed over a series of three parallel auroral arcs. The most poleward of the arcs was probably subvisual. The other two were not resolved in the DMSP imagery due to their spatial proximity and the slant of magnetic field lines.

References

1. Storey, L.R.O. (1963) The design of an electric dipole antenna for VLF reception within the ionosphere, Tech. Rep. No. 308 TC, Centre National d'Etudes des Telecommunication, Paris.
2. Fahleson, U.V. (1967) Theory of electric field measurements conducted in the magnetosphere with electric probes, Space Sci. Rev. 7:238.
3. Smiddy, M., Kelley, M.C., Burke, W., Rich, F., Sagalyn, R., Shuman, B., Hays, R., and Lai, S. (1977) Intense poleward directed electric fields near the ionospheric projection of the plasmapause, Geophys. Res. Lett. 4:543.
4. Burke, W.J., Kelley, M.C., Sagalyn, R.C., Smiddy, M., and Lai, S. (1979) Polar cap electric field structures with a northward interplanetary magnetic field, Geophys. Res. Lett. 6(No. 1):21-24.
5. Morel, P.R., Hanser, F.A., and Sellers, B. (1975) Design Fabrication and Integration of an Electrostatic Analyzer for a Satellite Payload, AFCRI-TR-75-0017.
6. Rich, F.J., and Wildman, P.J.L. (1977) A Model for the Electrical Current Collected by a Planar Aperture Ion Collected with a Partially Blocked Field of View, AFGL-TR-77-0096, AD A040919.
7. Wildman, P.J.L. (1976) Studies of Low-energy Plasma Motion: Results and a New Technique, AFGL-TR-76-0168, AD A030333.
8. Wildman, P.J.L. (1977) A low energy ion sensor for space measurements with reduced photosensitivity, Sp. Sci. Inst. 3:363.
9. Taylor, H.A. (1972) The light ion trough, Planet. Space Sci. 20:1953.
10. Fletcher, R., Powell, M.J.D. (1964) A rapidly convergent descent method for minimization, Computer Journal 6:163.
11. Ackerson, K.L., and Franck, L.A. (1972) Correlated satellite measurements of low energy electron precipitation and ground based observations of a visible auroral arc, J. Geophys. Res. 77:1128.

12. Langel, R.A. (1975) A comparison of electric and magnetic field data from the OGO 6 spacecraft, J. Geophys. Res. 80:4661.
13. Schunk, R.W., Raitt, W.J., and Banks, P.M. (1975) Effect of electric fields on the daytime high latitude E and F regions, J. Geophys. Res. 80:3121.
14. Chappell, C.R., Harris, K.K., and Sharp, G.W. (1970) A study of the influence of magnetic activity on the location of the plasmapause as measured by OGO 5, J. Geophys. Res. 75:50.
15. Lui, A.T.Y., Venkatesan, D., Anger, C.D., Akasofu, S.-I., Heikkila, W.J., Winningham, J.D., and Burrows, J.R. (1977) Simultaneous observations of particle precipitation and auroral emissions by the ISIS 2 satellite in the 19-24 MLT sector, J. Geophys. Res. 82:2210.
16. Iijima, T., and Potemera, T.A. (1978) Large-scale characteristics of field-aligned currents associated with substorms, J. Geophys. Res. 83:599.
17. Burke, W.J., Donatelli, D.E., and Sagalyn, R.C. (1978) INJUN 5 observations of low-energy plasma in the high latitude topside ionosphere, J. Geophys. Res. 83:2047.
18. Anderson, H.R., and Vondrak, R.R. (1975) Observations of Birkeland currents at auroral latitudes, Ref. Geophys. Sp. Phys. 13:243.
19. Kindel, J.M., and Kennel, C.F. (1971) Topside current instabilities, J. Geophys. Res. 76:3065.
20. Shawhan, S.D., Falthammer, C.G., and Block, L.P. (1978) In the nature of large auroral zone electric fields at $1 R_E$ altitude, J. Geophys. Res. 83:1049.
21. Rees, M.H. (1963) Auroral ionization and excitation by incident energetic electrons, Planet Sp. Sci. 11:1209.
22. Bostrom, R. (1964) A model of auroral electrojets, J. Geophys. Res. 69:4983.
23. Torbert, R.B., and Mozer, F.S. (1978) Electrostatic shocks as the source of discrete auroral arcs, Geophys. Res. Lett. 5:135.

Appendix A

Electric Field Components at 60647 UT

In this Appendix, we calculate the components of the electric field at 60647 UT, using measurements by the ion drift meter to determine the component in the spin plane that is \perp to \vec{B} . A schematic of the sensors 1, 2, and 3 (Figure 15) shows that at this time sensor 2 was pointing close to the direction of the satellite's velocity vector. The currents to sensors 1 and 3 are

$$I_1 = -Nq\vec{V}_p \cdot \hat{n}_1 \quad (A1)$$

$$I_3 = -Nq\vec{V}_p \cdot \hat{n}_2$$

where N is the plasma density; \vec{V}_p is the total plasma velocity in the rest frame of the satellite; \hat{n}_1 and \hat{n}_3 are unit vectors normal to the apertures of sensors 1 and 3:

$$\hat{n}_1 = \cos 40^\circ \hat{x} - \sin 40^\circ \hat{y} \quad (A2)$$

$$\hat{n}_3 = \cos 40^\circ \hat{x} + \sin 40^\circ \hat{y}$$

In the satellite's frame of reference, the plasma bulk motion has three terms:

1. The satellite motion relative to an earth centered inertial system. At 60647 UT

$$\vec{V}_s = 7.05 \hat{x} + 0.15 \hat{y} \text{ (km/sec)} \quad (A3)$$

2. The corotational plasma drift

$$\vec{V}_c = -\Omega_{\oplus} r \sin \lambda \hat{y} = -0.5 \hat{y} \text{ km/sec} \quad (\text{A4})$$

where $\Omega_{\oplus} = 7.3 \times 10^{-5} \text{ sec}^{-1}$ is the earth angular speed; $r = 7.7 \times 10^3 \text{ km}$ is the satellite's distance from the earth's center, and $\lambda = 65.5^\circ$, the geographic latitude of the subsatellite point on the earth's surface V_c .

3. The cross-spin plane drift due to the component of E in the spin plane that is \perp to B ($E_{p\perp}$).

$$\vec{V}_E \simeq (E_{p\perp}/B) \hat{y} \quad (\text{A5})$$

Substituting (A2) to (A5) into (A1) and forming the ratio $I_1/I_3 = \xi$, we obtain

$$\frac{E_{p\perp}}{B} = \frac{1.09\xi - 1}{0.124(1 + \xi)} \quad (\text{A6})$$

At 60646 UT and 60647 UT, ξ had values of 1.45 and 1.05, respectively. The electric field at 60646 UT was 30 mV/m. Substitution of the values of ξ at 60646 UT and 60647 UT as well as $E_{p\perp}$ at 60646 UT allows us to calculate $E_{p\perp}$ at 60647 UT

$$E_{p\perp} (60647 \text{ UT}) = 8.9 \text{ mV/m}.$$

Having determined $E_{p\perp}$, we find it now possible to estimate $E_{p\parallel}$, the component of the electric field in the spin plane that is parallel to B . To do this, we need to know the orientation of $E_{p\perp}$ and the dipole (Figure 16). The orientation of $E_{p\perp}$ is found by assuming that the value of $\Psi = 75^\circ$ calculated at 60645 UT is constant. The dipole orientation can be estimated by recognizing that the maximum excursion of ϕ_m occurred $\sim 0.3 \text{ sec}$ after $\phi_{v \times B}$ went through a maximum. The orientation of the $\vec{V} \times \vec{B}$ component in the spin plane is determined from the satellite altitude and the IGRF model. The satellite spin rate is $\sim 18^\circ$ per sec. Thus, the dipole has moved $\sim 6^\circ$ beyond its position at the $\phi_{v \times B}$ maximum. The angle between the dipole and the Z axis is $\sim 34^\circ$. From simple trigonometric considerations, it is seen that $E_{p\parallel} \simeq E_{p\perp} \tan 49^\circ = 10.2 \text{ mV/m}$.

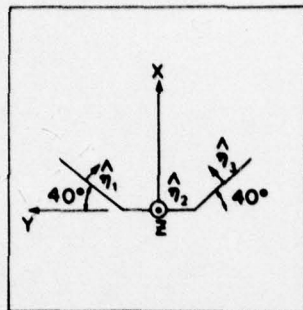


Figure 15. Schematic Representation of the S3-2 Ion Drift Meter Orientation at 60647 UT

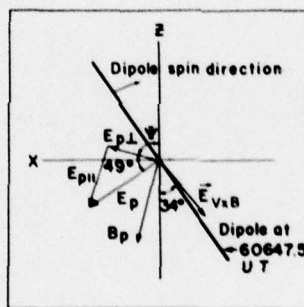


Figure 16. Orientation of the Electric Field Dipole at 60647.5 UT. The projections of the ambient E and B fields as well as the electric field due to the satellite motion are indicated